ACS OMEGA

http://pubs.acs.org/journal/acsodf

Article

The Reinforced Electromagnetic Interference Shielding Performance of Thermal Reduced Graphene Oxide Films via Polyimide Pyrolysis

Lijian Xu, Ledong Wang, Wenqian Zhang, Jie Xue, and Shifeng Hou*

Cite This: *ACS Omega* 2022, 7, 10955−10962

Read Online

ACCESS | Metrics & More | Article Recommendations | Supporting Information

ABSTRACT: In this work, thin reduced graphene oxide (GO) composite films were fabricated for electromagnetic interference (EMI) shielding application. High solid content GO slurry (7 wt %) was obtained by dispersing GO clay in polymer solution under high-speed mechanical stirring. A composite film with varied thickness (10−150 μm) could be fabricated in pilot scale. After an optimized thermal annealing procedure, the final product showed good conductivity, which reached 500 S·cm^{-1}. The thin sample (thickness < 0.1 mm) containing 10% polymer showed an enhanced EMI shielding performance of 55−65 dB. The outstanding EMI shielding efficiency as well as good suppleness and industrialized potential of thermal reduced graphene oxide polymer composite films could make a progress on their application in flexible devices as an EMI shielding material.

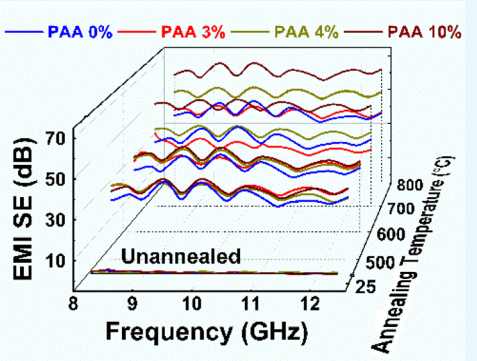

1. INTRODUCTION

Electromagnetic interference (EMI) is a common issue that can cause electron device failure.[1,2] Several kinds of materials are applied due to their EMI shielding performance according to different mechanisms.[3−5] The first-generation EMI shielding materials are metals such as Cu, Ni, Fe, and their alloys. They are usually applied as foil, foam, or bulk[6−10] and gradually replaced by composite shielding materials.[11−17] For the new member of carbon material, graphene shows several exceptional properties,[18] which make it possible to be used as an EMI shielding material.

Graphene could be assembled to different formations by various forming processes.[19−22] With the industrial scale production of graphene materials, many interesting results have been demonstrated by researchers using bulk graphene as the main component.[23−26] Another approach for the EMI shielding score is graphene derivatives[27] such as graphene/polymer composite[28−31] and graphene/metal oxide composite.[32−34]

Most of the reported work with satisfying EMI shielding performance could not be industrially amplified by the unmatched fabrication process due to low yield (usually less than the kilogram class), chemical risk (HI or hydrazine),[35,36] and high graphitization temperature (>2800 °C). In consideration of the balance between cost-effectiveness and expected performance, an optimized recipe and manufacturing process are necessary.

Herein, commercial graphene oxide (GO) was used as the main component to make thin composite films for EMI shielding application. By dispersing in polyamide acid (PAA) DMAc solution, the GO slurry showed compatibility with the pilot coating machine, while the range of slurry thicknesses on the PET matrix varied by its viscosity. The reduction of the graphene oxide sheets and the cyclization of polyimide occurred during the following optimized annealing process, which converted the insulative film into a conductive film. The annealed composite film showed better electrical conductivity and EMI shielding performance with the increase in anneal temperature, typically 500 S·cm^{-1} and 60 dB of the sample after 800 °C treatment with a thickness under 100 nm. The addition of the polymer component increased the toughness and EMI shielding performance of the annealed film. Both the simple composite process with low requirements of equipment and the satisfying EMI shielding performance of the composite film give a prospective commercial application of graphene material as an EMI shielding material.

2. RESULTS AND DISCUSSION

2.1. Preparation of Compound Slurry and Composite Films. GO could be well dispersed in many solvents due to its large specific area and abundant oxygenic groups attached to it. The selected solvents that could form a stable suspension with a wide GO content range were water, dimethylformamide (DMF), *N*-methyl pyrrolidone (NMP), and DMAc. DMAc was chosen in this work by its compatibility with polyamide

Received: November 30, 2021
Accepted: March 15, 2022
Published: March 24, 2022

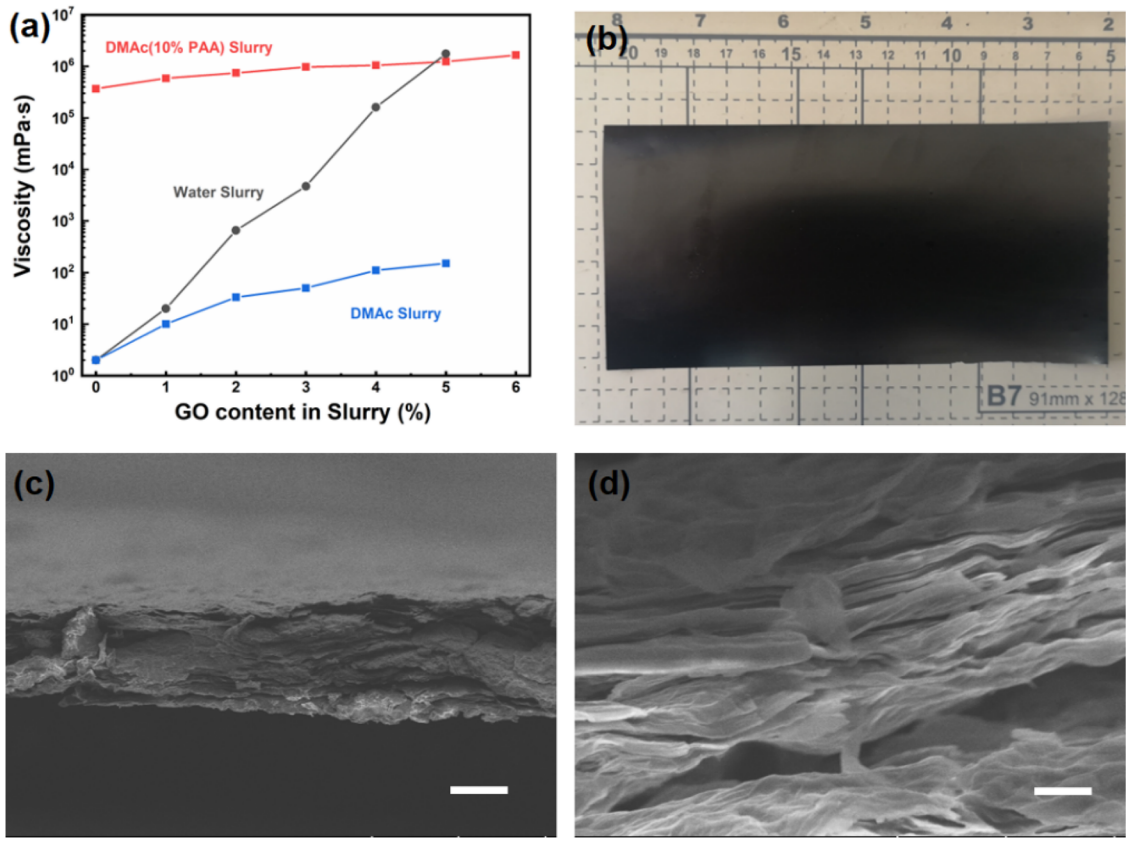

Figure 1. (a) Viscosity curves of compound slurries. (b) Digital photo of the tailored GO composite film. (c) Section view of the GO composite film, magnified ×1500; the scale bar is 50 μm. (d) Magnified section view of the GO composite film, magnified ×20,000; the scale bar is 2 μm.

acid to obtain a homogeneous compound slurry. The interaction between solvent molecules and solute was expressed as the apparent viscosity of the compounds. Figure 1a shows that the viscosity of the DMAc slurry, water slurry, and polymer solution slurry varied with the GO content. The water-based slurry showed the exponential increase in viscosity (coefficient of about 1) with the increase in solid content mainly because of the high hydrogen bond density. The viscosities of water-based slurry were 2400 mPa·s when the total solid content was 3.0 wt % and 160,000 mPa·s when the total solid content was 4.0 wt %. The DMAc slurry showed a low viscosity (<200 mPa·s) within the testing range, which means the weak interaction between graphene sheets. When PAA was diluted with DMAc to 10 wt %, the viscosity of solution was 360,000 mPa·s at 20 °C and increased with the addition of GO clay. The long polymer chain could form twist and tangled conformations due to the high concentration, which leads to the high viscosity. The addition of graphene oxide sheets did not improve the entanglement of polymer chains, but the $\pi-\pi$ interaction between graphene sheets and aromatic rings in the polymer chain could also enhance the interaction between solutes, which increased the apparent viscosity of the compounds. In the situation of very high GO content in slurry, the polymer chain may do some lubrication or separation between graphene sheets, so the compound slurry showed lower viscosity than water-based pure GO slurry.

The fabrication process of the GO/PAA composite film is illustrated in Scheme 1. Precoating test was done using small coating equipment. The slurries could form a flat coating on the PET film by shearing force. The solvent in a wet slurry coating vaporized by external heating to form a compact GO

Scheme 1. Fabrication Process of the GO-PAA Composite Film by the Coating Machine

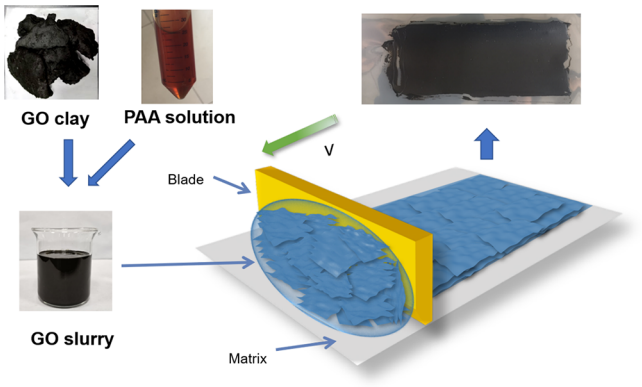

film as shown in Figure s1. The defects were caused by bubbles that were hard to eliminate inside the high-viscosity slurry. The best slurry recipe in our test was GOP10, which could form a smooth coating surface with few defects.

The remaining coating thickness after the drying process is equal to the slurry solid content, which is ideal for the conservation of mass, and a higher solid content should be better for final application. The thickness of the wet slurry coating was fixed to 1 mm, and the thickness and gross view of dried GOP3 and GOP10 composite films are shown in Figure s2. The gross view of composite films showed no significant difference in surface flatness and roughness, and the thickness of the remaining coating was a bit higher than the theoretical value due to the residual solvent. Because of the high viscosity,

https://doi.org/10.1021/acsomega.1c06767
ACS Omega 2022, 7, 10955−10962

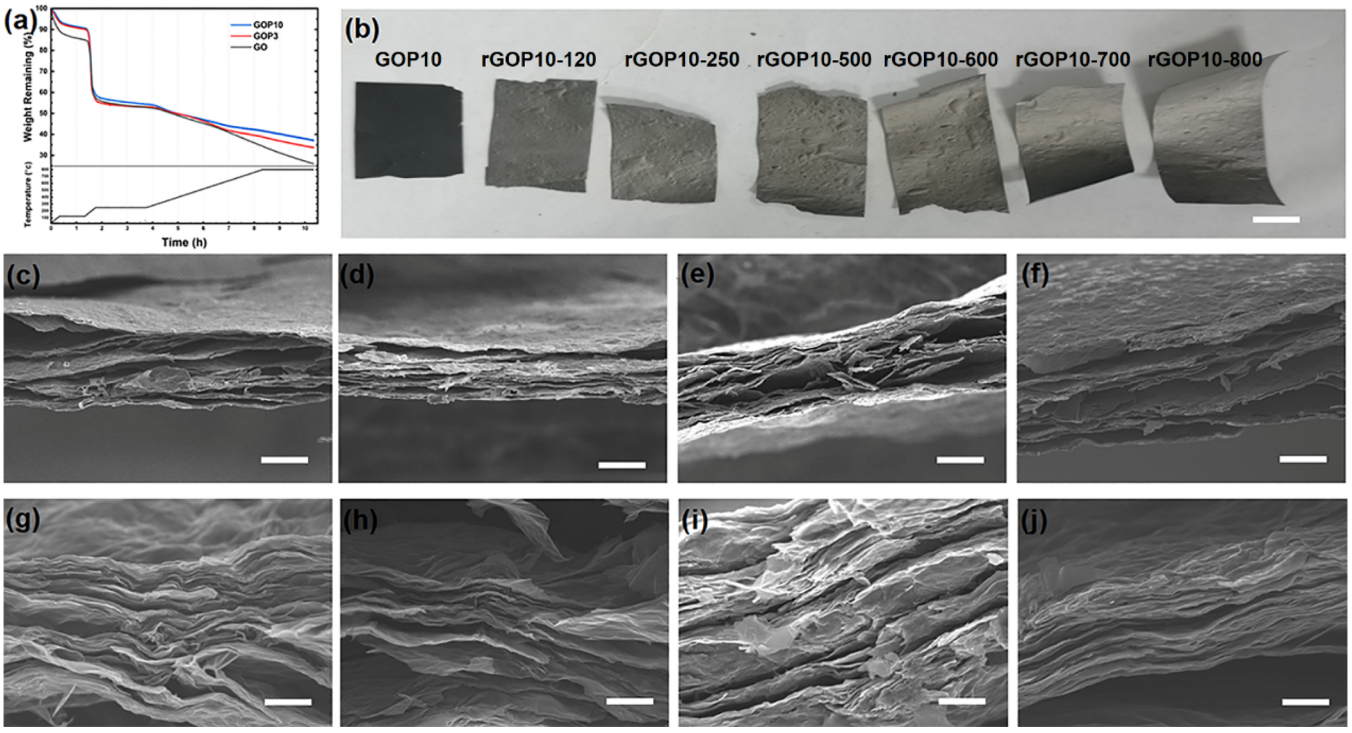

Figure 2. (a) TGA curves of GO, GOP3, and GOP10. (b) Appearance of the GO composite film after different annealing processes; from left to right: GOP10, rGOP10-120, rGOP10-250, rGOP10-500, rGOP10-600, rGOP10-700, and rGOP10-800. (c–f) Section view of rGOP10-500 (c), rGOP10-600 (d), rGOP10-700(e), and rGOP10-800 (f), magnified ×1500; scale bars are 50 μm. (g–j) Magnified section view of rGOP10-500 (g), rGOP10-600 (h), rGOP10-700 (i), and rGOP10-800 (j), magnified ×20,000; scale bars are 2 μm.

the slurry could form a stable coating with a thickness of 3 mm (upper limit of our equipment), which means that an ∼200 μm graphene film could be produced in pilot scale; this is a promising process for industrial application of graphene materials.

The section-view SEM images of GOP10 showed a compact structure without a cavity or defect. Also, few defects were observed on the sample's surface as shown in Figure 1c. The magnified image (Figure 1d) showed the tight arrangement of the smooth GO sheet caused by evaporation of solvent.

2.2. The Structure and Properties of Composite Films. The annealing process was optimized into several stages in this work, and TGA was employed to investigate the variation in this procedure. The TGA result showed the sample's weight change during the preparation of rGOP10-800, rGOP3-800, and rGO-800 (Figure 2a). The composite samples decreased to 90% of the initial weight during the first stage (1 h at 125 °C), which was less than the pure GO sample. After stage 2 (heated for 50 min to 250 °C and kept for 2 h), all samples decreased to 70% of the initial weight, which occurred mainly above 200 °C due to the pyrolysis of the carboxyl group on the outer GO lamella. For the following stage 3, a fixed time was set to reach the peak temperature and sustained for another 2 h. The interior GO sheets could get fully annealed by the decomposition of carboxyl, which showed a smooth weight loss. The pyrolysis of the polymer component did not contribute much to the total weight due to its less decomposition proportion under 500 °C (Figure S3). The weight loss of converted polyimide occurred above 600 °C, which is consistent with the improvement of the EMI shielding efficiency.

The difference between unannealed and treated samples is shown in Figure 2b. The unannealed composite film with a black appearance showed no bubbles. The annealed composite films showed graphite shine with mild bending or curling, which means that the films were reduced. The application of pure rGO film was limited by its frangibility in a free-standing situation, so polyimide was introduced into this system because of its high temperature resistance and natural toughness. The precursor PAA began converting into polyimide above 500 °C. Some bending and small humps were observed on the surfaces due to the asymmetry internal stress arisen during reduction. rGOP10-800 was in the same situation with rGOP10−250, which demonstrated that the appearance of the annealed films was not a qualification of graphitization. But the toughness of rGOP10-800 was extremely enhanced, which could bear extrusion or bending as shown in Video s1.

SEM images of rGOP10-500, rGOP10-600, rGOP10-700, and rGOP10-800 are shown in Figure 2c–j. The gaps between GO sheets in the treated samples were different from those of unannealed samples. The expansion of the composite film after thermal treatment occurred among all the recipes in our work, and the initial stack structure was split into several lamellas with varied gaps, while the increment in film thickness was enlarged by a higher peak temperature. For rGOP10-500 (Figure 2c), the cavities of different sizes were scattered among the lamellas; the ones near the surface were larger than interior ones and generated surface humps. In the magnified image of the central part (Figure 2g), the stacked sheets showed wrinkles and tunnels inside but were not separated. The gaps gained growth in both depth and range when the treatment temperature was raised; they could connect into a continuous space to form a multiple-layer structure (Figure 2f,j). The additional interfaces generated during the annealing process made better reduction of the composite material and also could promote some interfacial properties.

https://doi.org/10.1021/acsomega.1c06767
ACS Omega 2022, 7, 10955−10962

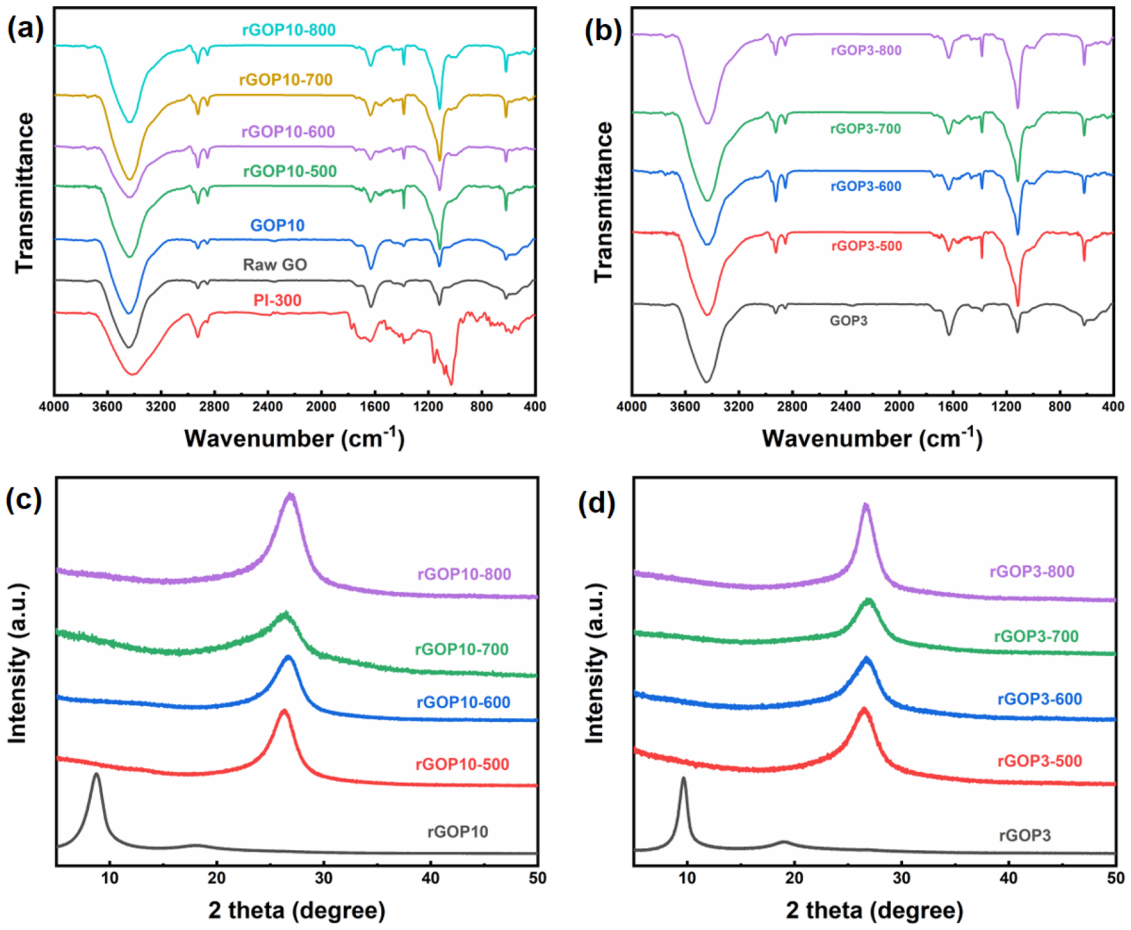

Figure 3. (a) FTIR spectra of rGOP10 series samples. (b) FTIR spectra of rGOP3 series samples. (c) XRD pattern of rGOP10 series samples. (d) XRD pattern of rGOP3 series samples.

The chemical variation of the composite film during the annealing process was detected by FTIR (Figure 3a,b). The absorption peak of the oxygenic group could be observed at 3446, 1630, and 1104 cm^{-1}, which belong to −OH, −COOH, and −C−O−C−, respectively. After thermal treatment, an obvious decrease of the −COOH peak (1630 cm^{-1}) was observed, while the broad −OH (3440 cm^{-1}) peak did not change much, which means that the great weight loss was mainly caused by the decomposition of carboxyl.

C−H bending generated a peak located at 1385 cm^{-1} on the spectra of decarboxylated samples. While being treated at a higher temperature, a peak at 1104 cm^{-1} was strengthened by the newly generated −C−O−C− from adjacent −OH. For samples annealed at 500 °C, a higher C−H peak was observed, which occurred due to the attachment of intermediate amorphous carbon on the graphene sheets. When the annealing temperature increased, those unstable non-aromatic carbons may get removed and showed a decreased −C−H peak. Most of oxygenic groups especially carboxyl could be removed by the staged thermal treatment process, with remaining oxygen existing as epoxy or hydroxyl. Element analysis also supports deoxygenation (Table 2).

Table 1. Some Parameters of the Composite Films

sample	thickness (mm)	conductivity ($S \cdot cm^{-1}$)	element components (%) N (%)	C (%)	H (%)	S (%)
GO	0.076		0.02	47.17	3.03	0.32
PI			9.50	68.07	3.21	0.16
GOP10	0.078	0.1	2.91	53.01	3.48	0.37
rGOP10-500	0.076	200	4.29	84.40	1.44	0.36
rGOP10-600	0.072	333	3.98	88.35	1.33	0.45
rGOP10-700	0.078	500	3.91	91.26	1.33	0.34
rGOP10-800	0.082	500	4.28	91.81	1.60	0.34

Table 2. Recipe of the GO/PAA Composite Film (phr.)

recipe mark	GO clay (solid content, 45%)	PAA solution (solid content, 17%)	DMAC (AR grade)
GO	9.5	0	100
GOP3	9.5	3	100
GOP4	9.5	4	100
GOP10	9.5	10	100

Figure 3c,d displays the XRD pattern of the composite film and treated ones. It can be seen that the unannealed composite film showed a strong peak located at $2\theta = 9.70°$ and a small peak at $2\theta = 18.93°$, which proved that the initial GO was fully separated into a single sheet, while the GO sheets were simply stacked during film fabrication. The sample rGOP3 showed a significant shift to a peak near $2\theta = 26.5°$ (002 of graphite) and

https://doi.org/10.1021/acsomega.1c06767
ACS Omega 2022, 7, 10955−10962

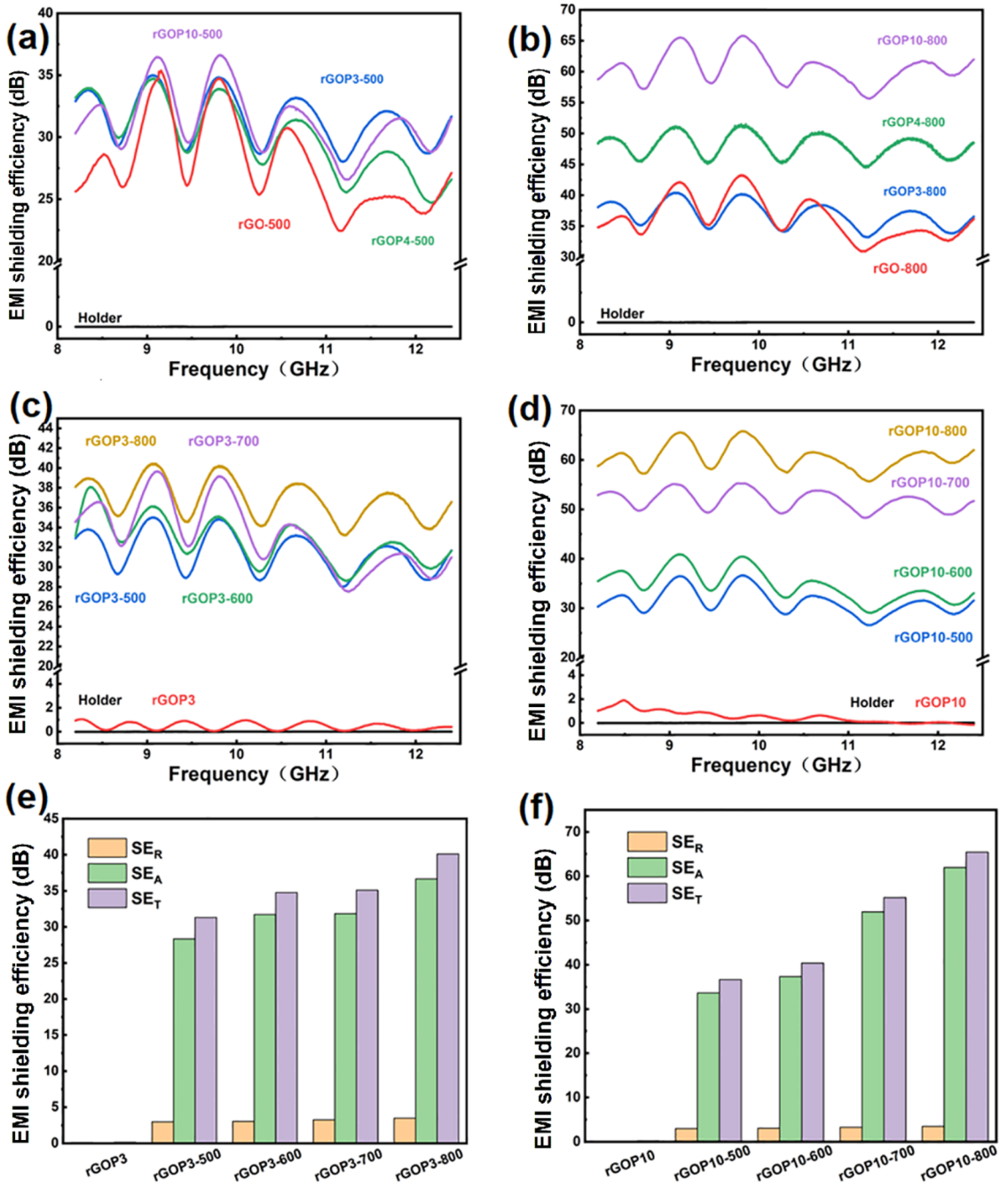

Figure 4. (a, b) EMI SE of different composite films annealed at 500 °C (a) and 800 °C (b). (c, d) EMI SE of rGOP3 series samples (c) and rGOP10 series (d) annealed at different temperatures. (e, f) EMI SE component of rGOP3 series samples (e) and rGOP10 series samples (f).

indicated the reduction of GO. rGOP3-500 and rGOP3-600 showed a peak located at 2θ = 26.46°, while the peak got a little shift by the annealing process above 700 °C (2θ = 26.60° of samples rGOP3-700 and rGOP3-800). These were another proof of deoxygenation. For more polyimide-containing composite films, the unannealed sample GOP10 showed a larger gap between the sheets with the expression of a strong peak located at 2θ = 8.78° and a weak peak located at 2θ = 18.14°, which are probably due to the insertion and adsorption of the polymer chain. After the thermal annealing process, the rGOP10 samples were fully reduced by the decomposition of graphene oxide and polymer, and the residual got a similar diffraction pattern to rGOP3 or other rGO samples, which means that they have a similar microstructure.

2.3. The EMI Shielding Performance of Composite Films. The conductivity of the composite film was obviously improved by the annealing process when the insulated part of the GO sheet was removed. The higher the annealing temperature applied to the films, the better the conductivity of the films. The polymer content did not affect the final result of conductivity as rGOP3-800 and rGOP10-800 both showed a conductivity of 500 $S \cdot cm^{-1}$, which was much larger than the samples treated under a lower temperature.

A vector network analyzer was employed to check the EMI shielding efficiency (SE) of composite samples (waveguide method, 8.2−12.4 GHz, room temperature). All samples show satisfying EMI SE with mild floating within the testing frequency range. The results showed the relevance to annealing

https://doi.org/10.1021/acsomega.1c06767
ACS Omega 2022, 7, 10955−10962

temperature and film composition. In total, the maximum EMI shielding efficiency of each sample appeared at 9.3 and 9.8 GHz, and the EMI shielding efficiency was dramatically improved as a higher temperature was applied during the annealing process, while the high polymer content led to high EMI shielding efficiency. The EMI shielding efficiency of samples annealed at 500 °C exceeded the commercial requirement standard value of 20 dB; the untreated composite films showed a little higher shielding efficiency than the pure rGO film (Figure 4a). When the peak annealing temperature increased to 800 °C, the composite samples showed the significant enhancement of the EMI shielding efficiency by the addition of polymer content (Figure 4b). The maximum EMI SE of rGOP10-800 is as high as 65 dB at 9.8 GHz, which is better than some other reported work (Table S1); rGOP4-800 shows an EMI SE of 50 dB at 9.8 GHz, which is still higher than that of the pure rGO film, but rGOP3-800 showed similar performance to the pure rGO film, which indicate the lower limit of the polymer content for the reinforcement of EMI shielding property.

The effect of annealing temperature was studied, and the results of rGOP3 and rGOP10 series are shown in Figure 4c,d. The unannealed composite film showed little EMI shielding performance, which is under 2 dB in the whole X-band. The rGOP3 samples showed less variation of EMI shielding efficiency by the increase in anneal temperature; rGOP3-800 showed a maximum EMI SE of ∼40 dB at 9.2 GHz and rGOP3-500 showed an EMI SE value of ∼35 dB. For rGOP10 samples, the EMI shielding efficiency was reinforced obviously, and the maximum EMI SE of rGOP10-500 was ∼36 dB at 9.8 GHz, while rGOP10-700 showed a value of ∼55 dB and rGOP10-800 showed a value of ∼65 dB. Figure 4e,f reveals an obvious tendency on the variation of each SE component. For the rGOP3 series sample (Figure 4e), the total shielding efficiency (SE_T) was the cumulation of reflection (SE_R) and absorption (SE_A), the SE_R shows little variation with the anneal temperature changes, and the increase in SE_T was mostly contributed by SE_A, which means that more incident waves were absorbed by the multilayer composite film containing some formations converted from the polymer component. For rGOP10 series, the situations remain the same (Figure 4f). The reflection was associated with electrical conductivity, and all the annealed composites showed a similar conductivity of ∼500 $S{\cdot}cm^{-1}$ and a similar SE_R value.[37] With the difference derived from the variation of polymer content, the higher the polymer content, the better the EM wave absorption that occurred. The first polymer component was polyamide acid until the annealing process; cyclization of polyamide acid occurred during the previous stages of the annealing process and it transformed into polyimide. The polymer chain may carbonize and rearrange into a graphite lattice structure as the temperature increased;[38−42] this situation has been applied to fabricate a highly thermally conductive graphene film under harsh conditions such as high temperature and high pressure, which are the main obstacles of continuous and large-scale fabrication. The conversion of polyimide during the annealing process under 800 °C may be due to the template effect of reduced graphene sheets nearby, but the mechanism is still unclear, which needs more investigations. But the reinforcement of the EMI shielding efficiency reaches a satisfying level, which is further better than the commercial requirement, so the composite process could be applied in the engineering fabrication.

3. CONCLUSIONS

In conclusion, we have demonstrated the fabrication of a GO-PAA composite film and their good EMI shielding performance after optimized thermal treatment. The thickness of the composite film ranged from 10 to 200 μm by a compatible coating machine. The deoxygenation of the composite film occurred during thermal treatment and reduced the GO sheet; the final product got an improved conductivity of 500 $S{\cdot}cm^{-1}$. The samples showed enhanced EMI performance by increasing the annealing temperature and polymer content. The best recipe for the composite film was 30% polymer content and annealing at 800 °C in our work; rGOP10-800 showed an EMI SE of 55−65 dB in the X-band. Also, the enhanced toughness of the composite film makes it available for flexible device application. For the excellent performances and operability to expanded production, the composite film may get an achievement as EMI shield materials.

4. EXPERIMENTAL SECTION

4.1. Materials. GO clay (solid content, 45%) was obtained from LeaderNano Co., Ltd. The PET film was purchased from Tmall.com. Dimethylacetamide (DMAc, AR) was purchased from Sinopharm Chemical Reagent Co., Ltd. The polyimide precursor (SS-2, polyamide acid in DMAc; solid content, 17%) was purchased from Jiangsu Shino New Materials Technology Co., Ltd.

4.2. Preparation of the GO/PAA Composite Film. PAA solution was prediluted with DMAc and then compounded with a calculated weight (details in Table 1) of graphene oxide clay in a double planet mixer. The staged compounding procedure occurred for 24 h under variable mixing speed (30−120 rpm) and shearing speed (1500−8000 rpm) with continuous cooling. The prepared slurry was transferred to the coating system after 6 h of settlement. For the whole coating system, the width of the PET film matrix was 350 mm and the width of the working area was 250 mm; the coating thickness was fixed to 1 mm. The prepared GO/PAA composite film was exfoliated manually for further processing.

4.3. Thermal Treatment of the GO/PAA Composite Film. The prepared composite film was kept for 24 h in a 125 °C oven to remove residual solvent. A tubular annealing furnace was employed to accomplish thermal reduction of the precut composite film. The polyimide conversion and GO reduction both occurred during the staged annealing process. The increasing speed of previous stages (<250 °C) was 5 °C per minute and varied by different target peak temperatures in latter stages. The samples stayed at the peak temperature for 4 h and then cooled to room temperature by 10 °C per minute. The treated samples were labeled as rGOP*x*-*y* or rGO-*y* (pure GO samples), where *y* represents the peak anneal temperature. The total anneal process was operated under argon protection.

4.4. Characterization. The microstructures of the composite film were observed by SEM (SU8010, Hitachi). A rotating viscometer (RVDV-1, Shanghai FangRui Instrument) was used to check the viscosity of compound slurries. X-ray diffraction (XRD) was performed by an X-ray diffractometer (SmartLab 9KW, Rigaku, λ = 1.54 Å). A Fourier transform infrared spectrometer (Tensor II, Bruker) was employed to check the infrared spectrum. Thermogravimetric analysis was performed by a TGA 2 under an argon atmosphere. The electrical conductivity of the composite sample was measured by an RTS-9 four-probe test system (4 Probe Tech).

https://doi.org/10.1021/acsomega.1c06767
ACS Omega 2022, 7, 10955−10962

4.5. Assessment of EMI Performance. A vector network analyzer (Ceyear 3672B, CETC) was applied to measure the microwave scatter parameters (S11, S12, S21, and S22) in the frequency range of 8.2−12.4 GHz. The samples were tested by the waveguide method and precut as a rectangular plate with 25.0 mm length and 12.0 mm width. The sample was sandwiched at 0 position from port 1 inside a 100 mm sample holder. The incident power of electromagnetic wave was 0 dBm corresponding to 1 mW. The values of total shielding effectiveness (SE_T), SE absorption (SE_A), and SE reflection (SE_R) were calculated by following formulas:[43]

$$R = |S_{11}|^2 \quad (1)$$

$$T = |S_{21}|^2 \quad (2)$$

$$A = 1 - R - T \quad (3)$$

$$SE_T\ (dB) = -10\log(T) \quad (4)$$

$$SE_R\ (dB) = -10\log(1 - R) \quad (5)$$

$$SE_A\ (dB) = -10\log\left(\frac{T}{1 - R}\right) \quad (6)$$

where R denotes the reflection coefficient, T denotes the transmission coefficient, and A denotes the absorption coefficient.

■ ASSOCIATED CONTENT

Supporting Information

The Supporting Information is available free of charge at https://pubs.acs.org/doi/10.1021/acsomega.1c06767.

Photos of wet slurry coating; composite film appearance; TGA curve of pure PAA; results of dielectric constant test; apparent density data; reported EMI SE of different materials in the X-band (PDF)

Excellent flexibility of rGOP10-800(MP4)

■ AUTHOR INFORMATION

Corresponding Author

Shifeng Hou − *School of Chemistry and Chemical Engineering, Shandong University, Jinan, Shandong 250100, P. R. China;* orcid.org/0000-0001-7486-9153; Phone: +86-0531-88362815; Email: Shifenghou@sdu.edu.cn; Fax: +86-0531-88363180

Authors

Lijian Xu − *School of Chemistry and Chemical Engineering, Shandong University, Jinan, Shandong 250100, P. R. China*

Ledong Wang − *School of Physics, Shandong University, Jinan, Shandong 250100, P.R. China*

Wenqian Zhang − *School of Chemistry and Chemical Engineering, Shandong University, Jinan, Shandong 250100, P. R. China*

Jie Xue − *School of Chemistry and Chemical Engineering, Shandong University, Jinan, Shandong 250100, P. R. China*

Complete contact information is available at: https://pubs.acs.org/10.1021/acsomega.1c06767

Funding

This work was supported by the National Natural Science Foundation of China (grant 21475076).

Notes

The authors declare no competing financial interest.

■ REFERENCES

(1) Zhi, D.; Li, T.; Li, J.; Ren, H.; Meng, F. A review of three-dimensional graphene-based aerogels: Synthesis, structure and application for microwave absorption. *Composites, Part B* **2021**, *211*, 108642.

(2) Kruželák, J.; Kvasničáková, A.; Hložeková, K.; Hudec, I. Progress in polymers and polymer composites used as efficient materials for EMI shielding. *Nanoscale Adv.* **2021**, *3*, 123−172.

(3) Kumar, R.; Sahoo, S.; Joanni, E.; Singh, R. K.; Tan, W. K.; Kar, K. K.; Matsuda, A. Recent progress on carbon-based composite materials for microwave electromagnetic interference shielding. *Carbon* **2021**, *177*, 304−331.

(4) Song, W.; Cao, M.; Lu, M.; Bi, S.; Wang, C.; Liu, J.; Yuan, J.; Fan, L. Flexible graphene/polymer composite films in sandwich structures for effective electromagnetic interference shielding. *Carbon* **2014**, *66*, 67−76.

(5) Song, W.; Cao, M.; Fan, L.; Lu, M.; Li, Y.; Wang, C.; Ju, H. Highly ordered porous carbon/wax composites for effective electromagnetic attenuation and shielding. *Carbon* **2014**, *77*, 130−142.

(6) Wanasinghe, D.; Aslani, F. A review on recent advancement of electromagnetic interference shielding novel metallic materials and processes. *Composites, Part B* **2019**, *176*, 107207.

(7) Xu, Z.; Hao, H. Electromagnetic interference shielding effectiveness of aluminum foams with different porosity. *J. Alloy Compd.* **2014**, *617*, 207−213.

(8) Ji, K.; Zhao, H.; Zhang, J.; Chen, J.; Dai, Z. Fabrication and electromagnetic interference shielding performance of open-cell foam of a Cu−Ni alloy integrated with CNTs. *Appl. Surf. Sci.* **2014**, *311*, 351−356.

(9) Lee, H.-S.; Choe, H.-B.; Baek, I.-Y.; Singh, J. K.; Ismail, M. A. Study on the Shielding Effectiveness of an Arc Thermal Metal Spraying Method against an Electromagnetic Pulse. *Materials* **2017**, *10*, 1403−1410.

(10) Yang, S.; Chang, Y.; Hsieh, Y.; Lee, J. Electromagnetic shielding effectiveness of multilayer metallic thin film on plastic substrates. *J. Appl. Polym. Sci.* **2008**, *110*, 1403−1410.

(11) Singh, A. K.; Shishkin, A.; Koppel, T.; Gupta, N. A review of porous lightweight composite materials for electromagnetic interference shielding. *Composites, Part B* **2018**, *149*, 188−197.

(12) Wang, G.; Ong, S. J. H.; Zhao, Y.; Xu, Z. J.; Ji, G. Integrated multifunctional macrostructures for electromagnetic wave absorption and shielding. *J. Mater. Chem. A* **2020**, *8*, 24368−24387.

(13) Song, W.; Fan, L.; Cao, M.; Lu, M.; Wang, C.; Wang, J.; Chen, T.; Li, Y.; Hou, Z.; Liu, J.; Sun, Y. Facile fabrication of ultrathin graphene papers for effective electromagnetic shielding. *J. Mater. Chem. C* **2014**, *2*, 5057−5064.

(14) Abbasi, H.; Antunes, M.; Velasco, J. I. Recent advances in carbon-based polymer nanocomposites for electromagnetic interference shielding. *Prog. Mater. Sci.* **2019**, *103*, 319−373.

(15) Liang, L.; Xu, P.; Wang, Y.; Shang, Y.; Ma, J.; Su, F.; Feng, Y.; He, C.; Wang, Y.; Liu, C. Flexible polyvinylidene fluoride film with alternating oriented graphene/Ni nanochains for electromagnetic interference shielding and thermal management. *Chem. Eng. J.* **2020**, *395*, 125209.

(16) Gupta, S.; Tai, N.-H. Carbon materials and their composites for electromagnetic interference shielding effectiveness in X-band. *Carbon* **2019**, *152*, 159−187.

(17) Liu, H.; Wu, S.; You, C.; Tian, N.; Li, Y.; Chopra, N. Recent progress in morphological engineering of carbon materials for electromagnetic interference shielding. *Carbon* **2021**, *172*, 569−596.

(18) Luo, X.; Chung, D. D. L. Electromagnetic interference shielding reaching 130 dB using flexible graphite. *Carbon* **1996**, *34*, 1293−1294.

(19) Chen, Y.; Yang, Y.; Xiong, Y.; Zhang, L.; Xu, W.; Duan, G.; Mei, C.; Jiang, S.; Rui, Z.; Zhang, K. Porous aerogel and sponge composites: Assisted by novel nanomaterials for electromagnetic interference shielding. *Nano Today* **2021**, *38*, 101204.

(20) Liang, C.; Gu, Z.; Zhang, Y.; Ma, Z.; Qiu, H.; Gu, J. Structural Design Strategies of Polymer Matrix Composites for Electromagnetic Interference Shielding: A Review. *Nano-Micro Lett.* **2021**, *13*, 181.
(21) Wang, X.-Y.; Liao, S.-Y.; Wan, Y.-J.; Zhu, P.-L.; Hu, Y.-G.; Zhao, T.; Sun, R.; Wong, C.-P. Electromagnetic interference shielding materials: recent progress, structure design, and future perspective. *J. Mater. Chem. C* **2021**, *10*, 44−72.
(22) Singh, R. K.; Kumar, R.; Singh, D. P. Graphene oxide: strategies for synthesis, reduction and frontier applications. *RSC Adv.* **2016**, *6*, 64993−65011.
(23) Xi, J.; Li, Y.; Zhou, E.; Liu, Y.; Gao, W.; Guo, Y.; Ying, J.; Chen, Z.; Chen, G.; Gao, C. Graphene aerogel films with expansion enhancement effect of high-performance electromagnetic interference shielding. *Carbon* **2018**, *135*, 44−51.
(24) Huang, H.; Ming, X.; Wang, Y.; Guo, F.; Liu, Y.; Xu, Z.; Peng, L.; Gao, C. Polyacrylonitrile-derived thermally conductive graphite film via graphene template effect. *Carbon* **2021**, *180*, 197−203.
(25) Wang, Y.-Y.; Sun, W.-J.; Yan, D.-X.; Dai, K.; Li, Z.-M. Ultralight carbon nanotube/graphene/polyimide foam with heterogeneous interfaces for efficient electromagnetic interference shielding and electromagnetic wave absorption. *Carbon* **2021**, *176*, 118−125.
(26) Barani, Z.; Kargar, F.; Mohammadzadeh, A.; Naghibi, S.; Lo, C.; Rivera, B.; Balandin, A. A. Multifunctional Graphene Composites for Electromagnetic Shielding and Thermal Management at Elevated Temperatures. *Adv. Electron. Mater.* **2020**, *6*, 2000520.
(27) Kumar, P. Ultrathin 2D Nanomaterials for Electromagnetic Interference Shielding. *Adv. Mater. Interfaces* **2019**, *6*, 1901454.
(28) Shen, B.; Li, Y.; Yi, D.; Zhai, W.; Wei, X.; Zheng, W. Microcellular graphene foam for improved broadband electromagnetic interference shielding. *Carbon* **2016**, *102*, 154−160.
(29) Zhou, Y.; Wang, S.-j.; Li, D.-s.; Jiang, L. Lightweight and recoverable ANF/rGO/PI composite aerogels for broad and high-performance microwave absorption. *Composites, Part B* **2021**, *213*, 108701.
(30) Yu, Z.; Dai, T.; Yuan, S.; Zou, H.; Liu, P. Electromagnetic Interference Shielding Performance of Anisotropic Polyimide/Graphene Composite Aerogels. *ACS Appl. Mater. Interfaces* **2020**, *12*, 30990−31001.
(31) Zhang, C.; Lv, Q.; Liu, Y.; Wang, C.; Wang, Q.; Wei, H.; Liu, L.; Li, J.; Dong, H. Rational design and fabrication of lightweight porous polyimide composites containing polyaniline modified graphene oxide and multiwalled carbon nanotube hybrid fillers for heat-resistant electromagnetic interference shielding. *Polymer* **2021**, *224*, 123742.
(32) Kumar, R.; Sahoo, S.; Joanni, E.; Singh, R. K.; Tan, W. K.; Moshkalev, S. A.; Matsuda, A.; Kar, K. K. Heteroatom doping of 2D graphene materials for electromagnetic interference shielding: a review of recent progress. *Crit. Rev. Solid State Mater. Sci.* **2021**, 1−50.
(33) Kumar, R.; Macedo, W. C.; Singh, R. K.; Tiwari, V. S.; Constantino, C. J. L.; Matsuda, A.; Moshkalev, S. A. Nitrogen−Sulfur Co-Doped Reduced Graphene Oxide-Nickel Oxide Nanoparticle Composites for Electromagnetic Interference Shielding. *ACS Appl. Nano Mater.* **2019**, *2*, 4626−4636.
(34) Kumar, R.; Alaferdov, A. V.; Singh, R. K.; Singh, A. K.; Shah, J.; Kotnala, R. K.; Singh, K.; Suda, Y.; Moshkalev, S. A. Self-assembled nanostructures of 3D hierarchical faceted-iron oxide containing vertical carbon nanotubes on reduced graphene oxide hybrids for enhanced electromagnetic interface shielding. *Composites, Part B* **2019**, *168*, 66−76.
(35) Kumar, P.; Shahzad, F.; Yu, S.; Hong, S. M.; Kim, Y.-H.; Koo, C. M. Large-area reduced graphene oxide thin film with excellent thermal conductivity and electromagnetic interference shielding effectiveness. *Carbon* **2015**, *94*, 494−500.
(36) Wan, Y.-J.; Zhu, P.-L.; Yu, S.-H.; Sun, R.; Wong, C.-P.; Liao, W.-H. Graphene paper for exceptional EMI shielding performance using large-sized graphene oxide sheets and doping strategy. *Carbon* **2017**, *122*, 74−81.
(37) Colaneri, N. F.; Schacklette, L. W. EMI shielding measurements of conductive polymer blends. *IEEE Trans. Instrum. Meas.* **1992**, *41*, 291−297.
(38) Ferreira, F. A. S.; Battirola, L. C.; Lewicki, J. P.; Worsley, M. A.; Pereira-da-Silva, M. A.; Amaral, T.; Lepienski, C. M.; Rodrigues-Filho, U. P. Influence of thermal treatment time on structural and physical properties of polyimide films at beginning of carbonization. *Polym. Degrad. Stab.* **2016**, *129*, 399−407.
(39) Murakami, M.; Tatami, A.; Tachibana, M. Fabrication of high quality and large area graphite thin films by pyrolysis and graphitization of polyimides. *Carbon* **2019**, *145*, 23−30.
(40) Chen, X.; Deng, X.; Kim, N. Y.; Wang, Y.; Huang, Y.; Peng, L.; Huang, M.; Zhang, X.; Chen, X.; Luo, D.; Wang, B.; Wu, X.; Ma, Y.; Lee, Z.; Ruoff, R. S. Graphitization of graphene oxide films under pressure. *Carbon* **2018**, *132*, 294−303.
(41) Hatori, H.; Yamada, Y.; Shiraishi, M. In-plane orientation and graphitizability of polyimide films: II. Film thickness dependence. *Carbon* **1993**, *31*, 1307−1312.
(42) Wu, X.; Li, H.; Cheng, K.; Qiu, H.; Yang, J. Modified graphene/polyimide composite films with strongly enhanced thermal conductivity. *Nanoscale* **2019**, *11*, 8219−8225.
(43) Jiang, D.; Murugadoss, V.; Wang, Y.; Lin, J.; Ding, T.; Wang, Z.; Shao, Q.; Wang, C.; Liu, H.; Lu, N.; Wei, R.; Subramania, A.; Guo, Z. Electromagnetic Interference Shielding Polymers and Nanocomposites - A Review. *Polym. Rev.* **2019**, *59*, 280−337.

https://doi.org/10.1021/acsomega.1c06767
ACS Omega 2022, 7, 10955−10962